Volume 1 | Number 1 | Jan 2013 | Pages 1–100

Journal of
Materials Chemistry A

Materials for energy and sustainability
www.rsc.org/materialsA

Li⁺

e⁻

Li⁺

e⁻

Li⁺

Li⁺

ROYAL SOCIETY
OF CHEMISTRY

ROYAL SOCIETY
OF CHEMISTRY

www.rsc.org/materialsA

Chlorine-conducted defect repairment and seed crystal-mediated vapor growth process for controllable preparation of efficient and stable perovskite solar cells

Paifeng Luo,*[a] Zhaofan Liu,[a] Wei Xia,[a] Chenchen Yuan,[b] Jigui Cheng,[a] Chenxi Xu,[a] Yingwei Lu[a]

[a]Department of Materials Science and Engineering, Hefei University of Technology, Hefei, Anhui 230009, P.R. China

[b]CAS Key Laboratory of Materials for Energy Conversion, University of Science and Technology of China, Hefei, Anhui 230026, P.R. China

*corresponding author: Paifeng Luo

E-mail: lpfeng@hfut.edu.cn or lpfeng@mail.ustc.edu.cn

Tel: +86-551-62904566

Fax: +86-551-62905285

Abstract

Currently, Chlorine (Cl)-incorporated perovskite solar cells (PSCs) have triggered a strong interest due to their excellent crystallinity and charge transport property. Herein, we present a facile MaCl-assisted (Ma=CH$_3$NH$_3$) sequential tubular chemical vapor deposition (STCVD) method to fabricate perovskite films, and first report the novel Cl-conducted defect repairment and seed crystal-mediated vapor growth behavior. Further studies indicate that Cl has ultra-strong reaction capacity and special grain refining ability, and these unique features could effectively heal the inherent ditch defects on PbI$_2$ templates and overcome the blocking issue of incomplete conversion in perovskites. With the aid of Cl, the well-defined MaPbI$_{3-x}$Cl$_x$ small seed crystals are obtained and then grow up into compact, crack-free, and highly uniform MaPbI$_3$ layers with large grain size up to microscale. Accordingly, the big open-circuit voltage (V_{oc}) exceeding 1.0 V and high efficiency of 13.76% for our STCVD-processed PSCs measured without aperture mask are successfully achieved in this work. Strikingly, our perovskite device without encapsulation still has an efficiency of 4.15% even undergoing upon exposure to the ambient conditions for 1152 hour. Overall, we propose a viable strategy to realize the controllable preparation of PSCs, and also disclose the exact role of Cl in film morphology evolution during the Gas-Solid (G-S) growth process.

Key words: Defect repairment; Seed crystals; Vapor growth process; Controllable preparation; Perovskite solar cells

1. Introduction

Nowadays, development of photovoltaic industry has been widely adopted as one of the best solutions to relieve the global energy crisis.[1,2] However, both the 1st and 2nd generation photovoltaic devices (PVs), such as the dominated crystalline silicon, $CuInGaSe_2$ (CIGS) and CdTe thin-film solar cells, are still facing the challenges of cost reduction and process simplification.[3,4] Therefore, there is an urgent demand for fabricating cost-efficient solar cells through developing new material systems. Recently, the magic organic-inorganic hybrid perovskite family with a general formula $MaPbX_3$ (where Ma is the CH_3NH_3, and X is the halogen I, Br or Cl) has attracted much attention due to its high absorption coefficient, suitable direct band gap, excellent charge transport property, and high defect tolerance, which shows the potential as a cost-efficient alternative to traditional solar cells.[5-9] Based on the newcomer's outstanding optical-electric properties, substantial efforts have been devoted to the development of advanced manufacturing technologies for high performance PVs. Within the last several years, its power conversion efficiency (*PCE*) of PSCs has soared from 3.8% to 20.2%, which is assessed as one of the major breakthroughs in PV history.[10-17] However, the controllable preparation of PSCs is still critically challenging at current stage. It is very crucial for its morphology control since the PV performance is highly related to the film quality and crystal structure of perovskite materials, especially in the prevailing planar heterojunction configuration that encourages more homogeneous crystallization for high-efficient solar cells.[18-21] Thus deeply exploring and understanding the strong correlation between the film morphology evolution and its growth process is very essential to achieve high-quality perovksite layers for the further device performance enhancement.

In recent years, Cl-incorporated perovskites with excellent crystallinity and

charge transport property have triggered a strong interest in PSCs field.[22-26] In 2013, Snaith first reported that Cl incorporation can significantly increase the electron-hole diffusion length of $MaPbI_3$ films.[23] Subsequently, comprehensive morphological studies have been undertaken to elucidate the role of Cl, which is initially considered to have an immensely beneficial effect on the nucleation and crystallization of perovskites in the most studied solution process.[27-31] However, it is difficult to precisely control the film morphology as well as Cl incorporation in the uncontrolled liquid-phase growth process, where some unsolved problems often lead to the poor reproducibility and large variation on the device performance, such as the complex solution rheology, the incomplete conversion with a poor coverage, and the huge loss of volatile chloride at the extended annealing process.[32-36] On the contrary, high-quality perovskite films with Cl inclusion are readily achieved by vacuum evaporation route. Nonetheless, vacuum based technology requires expensive equipment investment and high energy consumption, which would hinder its future commercial applications.[37-38]

Lately, G-S crystallization process, vapor-assisted solution process (VASP), hybrid CVD, low-pressure CVD, and in-situ CVD, are consecutively developed by other researchers and our group, in which the slow G-S reaction could effectively retard the over-rapid intercalating reaction rate between inorganic frameworks and organic species, and avoid generating the rough and porous perovskite films.[34,39-43] Although vapor-assisted approaches have been considered as fruitful ways for fabrication of perovskites, too long duration time even exceeding 4 hours arising from the nature of slow G-S reaction should be satisfied to fulfill the complete conversion from inorganic templates to perovskites.[39] Meanwhile, small grains, apparent voids and cracks inevitably observed in $MaPbI_3$ layers by common vapor-assisted CVD

method significantly increase the charge recombination and result in a relatively low V_{oc} of 0.85~0.95 V, which should be attributed to the inherent ditch defects on PbI_2 templates and this issue will be discussed below.[39-42] Therefore, there is still lack of proper strategy to produce crack-free perovskite films and realize its controllable preparation by CVD approach. Meanwhile, admitting that the beneficial function of Cl is extensively studied in solution process, but thus far, no Cl is introduced into the vapor-assisted CVD approach, and its function of Cl in film morphology evolution remains as of yet unclear.

In this work, a novel MaCl-assisted two-step STCVD method is developed to fabricate perovskite films, and the open question about the exact role of Cl during the G-S growth process is first disclosed. Without the need of a glove box or expensive vacuum instrument, cost-efficient tubular CVD furnace is employed here, which could be readily scaled up for commercial mass production. Based on this facile STCVD process, Cl is skillfully introduced into $MaPbI_3$ perovskites during the vapor-assisted growth process. More importantly, it is found that Cl has ultra-strong reaction capacity and special grain refining ability, which may effectively repair the inherent ditch defect on PbI_2 templates and further fulfill the complete conversion. With the assistance of Cl, crack-free and highly uniform perovskite layers with ultra-large grains are obtained. As such, the charge recombination in grain boundaries (GBs) is tremendously reduced and the PV performance is significantly enhanced. Comparing with common CVD, the device V_{oc} via STCVD boosts from 0.915 V to 1.001 V, with an impressive enhancement of 86 mV. And the best efficiency tested without aperture mask is also greatly improved from 10.29% to 13.76%, demonstrating a high efficiency among CVD processed PSCs. Notably, as-prepared device without encapsulation exhibits a good stability in air environment. Therefore,

the desired controllable fabrication procedure for efficient and stable PSCs has been elucidated in this work, and our research sheds light on understanding the exact role of Cl in the G-S growth process of perovskite layers.

2. Results and discussion

2.1 Reaction ability of MaCl with PbI$_2$ templates

In order to reveal the function of Cl during G-S growth process, the intercalating reaction and its crystal structure evolution are investigated here through comparing the reaction abilities of MaI and MaCl with PbI$_2$ templates at different reaction stages. **Fig. 1** shows the (a, b) Photographs, (c, d) X-ray diffraction (XRD) patterns, and (e, f) UV-vis spectra of PbI$_2$ films reacted with MaI at 145 ^{o}C and MaCl at 120 ^{o}C for different duration time: 0 min, 5 min, 15 min, and 35 min, respectively. Yu *et al.* have demonstrated that MaCl is much easier to turn into gaseous phase as compared to MaI.[35] So due to the different sublimation temperatures, we separately set reaction temperatures of MaI at 145 ^{o}C and MaCl at 120 ^{o}C. In the case of MaI, even at higher temperature, the intercalating reaction rate between MaI and PbI$_2$ templates is quite slow, as can be seen from the color change in **Fig. 1** (a). When the reaction proceeds for 5 min, there is no crystal structural evolution from XRD in **Fig. 1** (c). The onset of UV-vis absorbance spectrum (**Fig. 1** (e), red line) also locates at the same position with that of PbI$_2$. Only when it reacts for 15 min, tetragonal MaPbI$_3$ perovskite phase is observed from XRD, showing peaks at 14.01^o, 28.19^o, 31.59^o, and 43.09^o, separately assigned as (110), (220), (310) and (330) planes.[8,22,26] Even then, we could clearly notice the presence of PbI$_2$ reflections at 12.61^o, which means the structural conversion from PbI$_2$ to MaPbI$_3$ is not complete.[8,35,44] That said, a rather long duration time is necessary to fulfill the complete transformation via kinetically unfavorable van
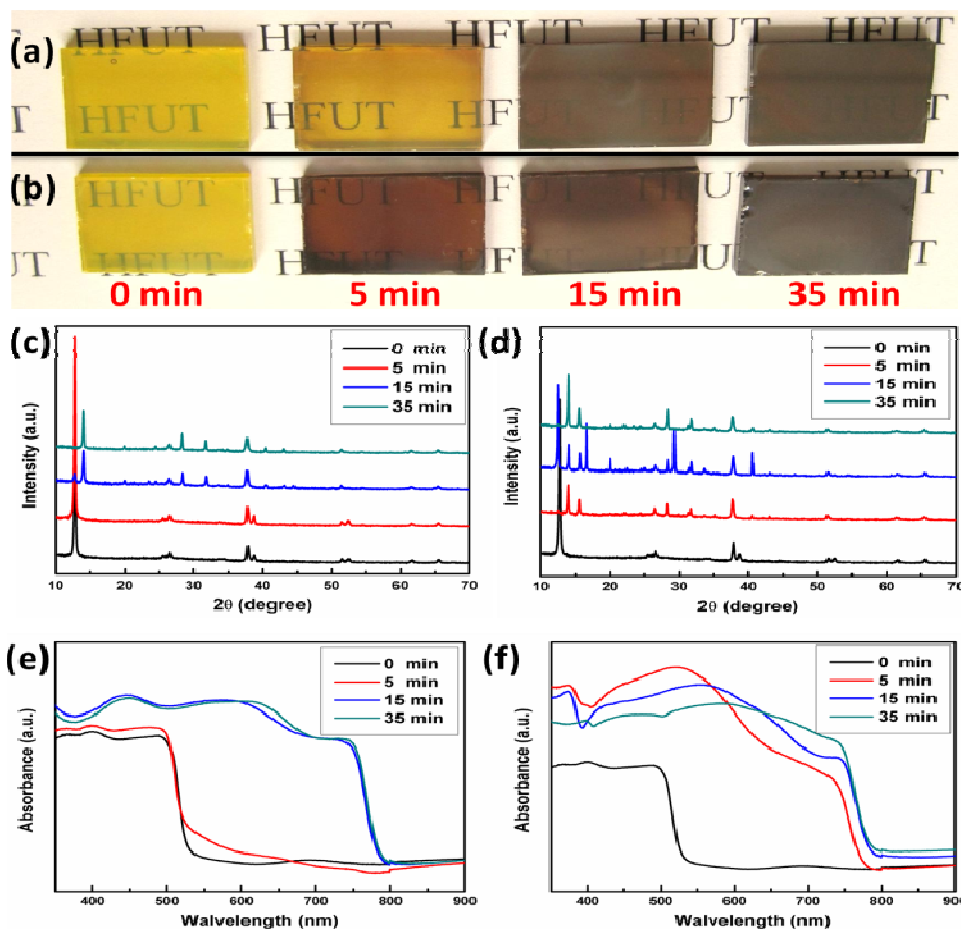
Fig. 1 (a, b) Photographs, (c, d) XRD patterns, and (e, f) UV-vis spectra of PbI_2 films reacted with MaI at 145 ^oC and MaCl at 120 ^oC for different duration time: 0 min, 5 min, 15 min, and 35 min, respectively.

der Waals gap.[41,45] Our results in MaI case are well consistent with Yang's observations, in which it even takes 2~4 hour to complete this conversion through VASP approach.[39]

On the contrary, from **Fig. 1** (b, d, f), we may see that MaCl is able to quickly react with PbI_2 even at lower temperature of 120 ^oC. Only reacted for 5 min, $MaPbI_{3-x}Cl_x$ perovskite structure has been formed rapidly, and no signals of PbI_2 are observed from XRD (**Fig. 1** (d), red line), and there is also a huge redshift visible in UV-vis spectra, which implies that complete conversion has been accomplished in such a short time. Here we infer that the fast reaction feature presumably comes from the ultra-strong penetrating power of Cl, and its small atomic radius facilitates the

diffusion into PbI_2 layered structure during G-S intercalating reaction process.[41] Note that the duration time in MaCl is a vital factor for the following seed crystal-assisted growth process. When it increases to 15 min, an interesting phase-splitting phenomenon appears from random diffractions (blue line) in **Fig. 1** (d), which should be attributed to the limited miscibility of $MaPbI_3$ and $MaPbCl_3$.[27,46] Thus 5 min's duration time in MaCl is very suitable for the growth of $MaPbI_{3-x}Cl_x$ seed crystals. Taken together, it is evident that MaCl has an ultra-strong reaction capacity with PbI_2, which could effectively solve the blocking issue and fulfill the complete conversion in perovskites.

2.2 Two-step STCVD reaction process

Based on the strong reaction ability of MaCl, a novel seed crystal-mediated two-step STCVD method is developed here. For comparison, (i) common CVD route abbreviated as R1 for ease and clarity and (ii) seed crystal-mediated STCVD route denoted as R2 are both depicted in **Scheme 1**. As shown in R1 only using MaI as vapor source, the slow G-S reaction between PbI_2 and MaI directly leads to too long duration time and incomplete conversion in perovskites.[39-42] At the same time, due to the inherent ditch defects on PbI_2 templates, as will be shown in the next part, uneven and porous film morphology is inevitably generated through the common CVD. Inversely, when MaCl is initially employed during first-step CVD process, it quickly reacts with PbI_2 and produces continuous $MaPbI_{3-x}Cl_x$ seed crystals with complete conversion in term of its strong reaction ability. In order to produce a large number of seed crystals for the following growth of high-quality perovskite films, we set the evolution time as 5 min just in case they grow too big and hardly convert back from $MaPbCl_3$ to $MaPbI_3$. As such, well-defined seed films then grow up to be compact $MaPbI_3$ layers under MaI vapor in second-step CVD process. Since Cl concentration
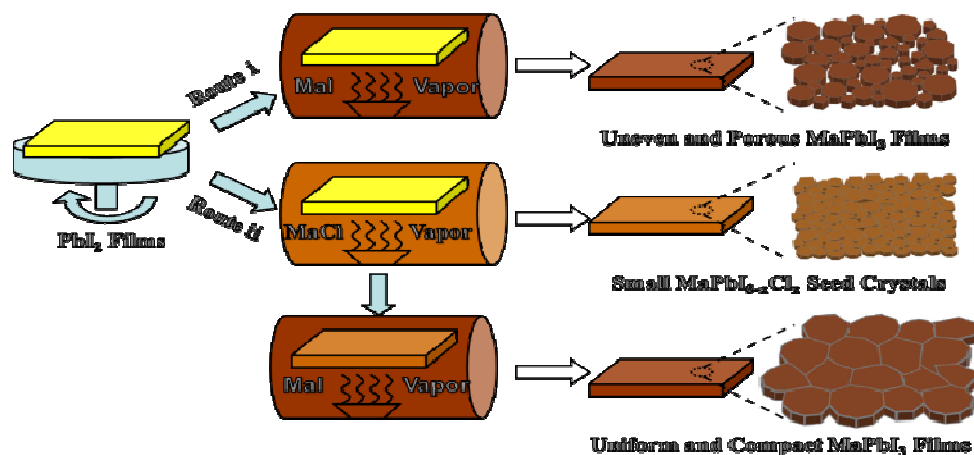
Scheme 1 Schematic growth processes of MaPbI$_3$ films by (i) common CVD and (ii) seed crystal-mediated STCVD.

in the final perovskite films is very low (<0.1 at%) and cannot be detected by the prevailing characterizations,[24,35,36] it is appropriate to use the formula "MaPbI$_3$" to denote its composition rather than the formula "MaPbI$_{3-x}$Cl$_x$". Hence our novel R2 recipe offers several incomparable advantages: Firstly, current solution process or vacuum evaporation requires complicated manipulations in glove box or expensive instrument investment, while our method is proceeded under open-air conditions employing the cost-efficient tubular CVD furnace, which is much more convenient to be applied in future large-scale applications. Secondly, the blocking issue of incomplete conversion in perovskites during solution based technology or common CVD process could be effectively solved by seed crystal-mediated STCVD method. Finally, all the operations in R2, including coating PbI$_2$ templates, growth of MaPbI$_{3-x}$Cl$_x$ seed crystals, and deposition of MaPbI$_3$ films, are easily manipulated and well controlled.

Then the crystal structure evolution as well as Cl incorporation in STCVD process is carefully scrutinized. **Fig. 2** shows (a) photographs and (b) crystal formation scheme of as-prepared PbI$_2$, MaPbI$_{3-x}$Cl$_x$, and MaPbI$_3$ films by R2. Here yellow PbI$_2$ precursor films are used as the precursor templates, then convert to brown
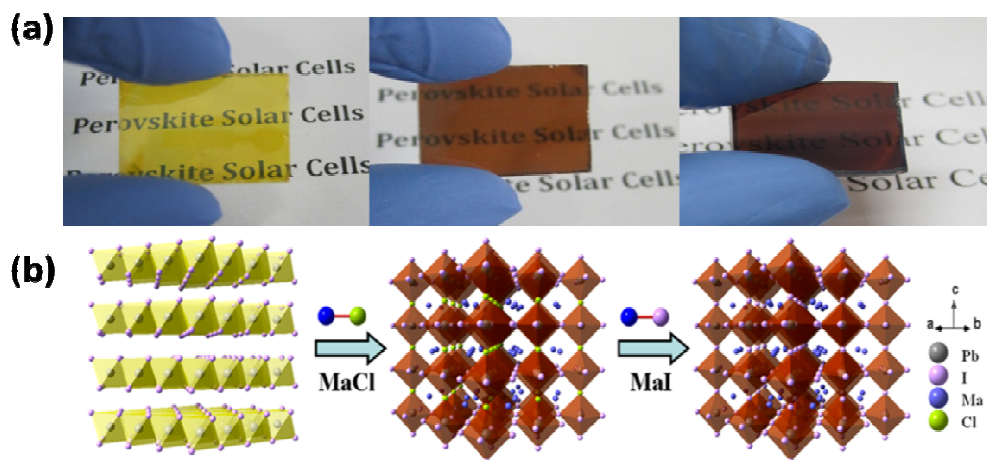
Fig. 2 (a) Photographs and (b) crystal formation scheme of as-prepared PbI_2, $MaPbI_{3-x}Cl_x$, and $MaPbI_3$ films by R2.

$MaPbI_{3-x}Cl_x$ seed films in MaCl vapor, and finally grow up to be dark brown $MaPbI_3$ layers in MaI atmosphere. The corresponding crystal structure evolution is also schematically drawn out and shown in this picture. Generally, as-spun PbI_2 films own a hexagonal structure with space group *P-3m1(164)*, and $MaPbI_3$ layers have a perovskite structure with space group *Pbnm(62)*.[41,47,48] During this typical intercalating reaction process, organic species are able to insert the layered PbI_2 inorganic templates with ease, and evolve as perovskites. For the case of MaCl, this reaction will carry out rapidly on account of the small radius of Cl, which is in agreement with the above experiments. Mosconi *et al.* perform periodic density funtion (DFT) calculations and suggest that Cl atoms are preferentially occupying the apical positions of PbI_6 octahedra.[30,46] Here we adopt this proposal and present the schematic structural diagram of $MaPbI_{3-x}Cl_x$ seed crystals, in which I atoms (purple color) are partially substituted by Cl atoms (green color) on the apical positions. In fact, the substituted amounts should be limited otherwise they more likely exist in the form of split phases as observed in previous XRD. Because both from experimentally and theoretically, it is hard to form continuous $MaPbI_{3-x}Cl_x$ solid phase and only occurs at a relatively low Cl content according the view of Colella.[24]
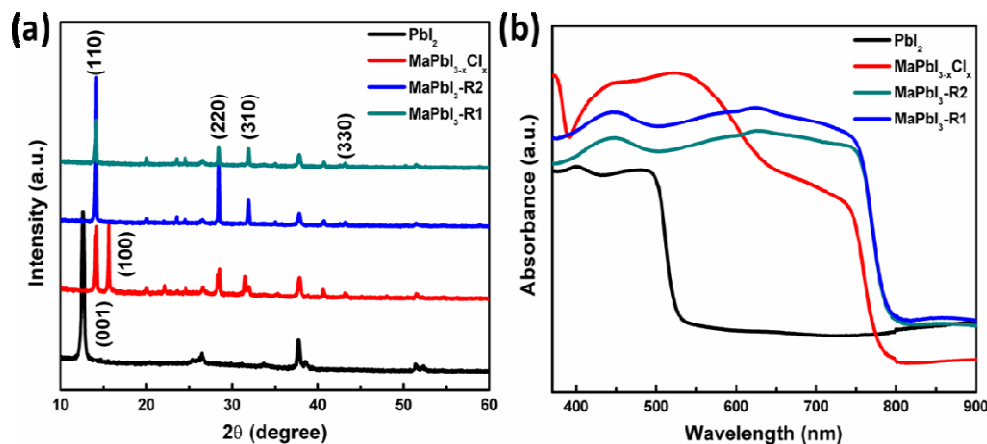
Fig. 3 (a) XRD patterns and (b) UV-vis spectra of PbI_2 (black line), $MaPbI_{3-x}Cl_x$ (red line) and $MaPbI_3$ (blue line) films by R2, and $MaPbI_3$ films by R1 (dark cyan line).

    Fig. 3 gives (a) XRD patterns and (b) UV-vis spectra of PbI_2 (black line), $MaPbI_{3-x}Cl_x$ (red line) and $MaPbI_3$ (blue line) films by R2, and $MaPbI_3$ films by R1 (dark cyan line). It is clear that both $MaPbI_3$ films by R1 and R2 exhibit identical perovskite crystal lattices with distinctive (110), (220), (310), and (330) diffractions, and also have similar absorption onsets at ~800 nm wavelength, which is in accordance with related works.[22,26,46] Comparing with R1, as shown in **Fig. S1**, $MaPbI_3$ films by R2 exhibit stronger diffraction intensity and higher absorbance, which means that our method could achieve high-quality perovskite films. Remarkably, we may confirm that Cl has been incorporated into perovskites from the peak position variations of preferred (110) orientation. As detected from XRD, the peak positions of $MaPbI_3$ films by R1 and R2, and $MaPbI_{3-x}Cl_x$ seeds are separately centered at 14.06^o, 14.16^o, and 14.20^o. With the increasing of Cl content, the peaks slightly shift to higher degrees, causing a little lattice distortion and the broadening of the full width at half maximum (FWHM) of (110) plane (**Fig. S1**), which is quite in agreement with other claims.[24,26,35] Meanwhile, $MaPbI_{3-x}Cl_x$ denoted as red lines in plots gives (001) peak at 15.62^o and absorbance at 785 nm, which once again attests to the Cl inclusion in perovskites.[35,44] To further study the issue of the presence of Cl,
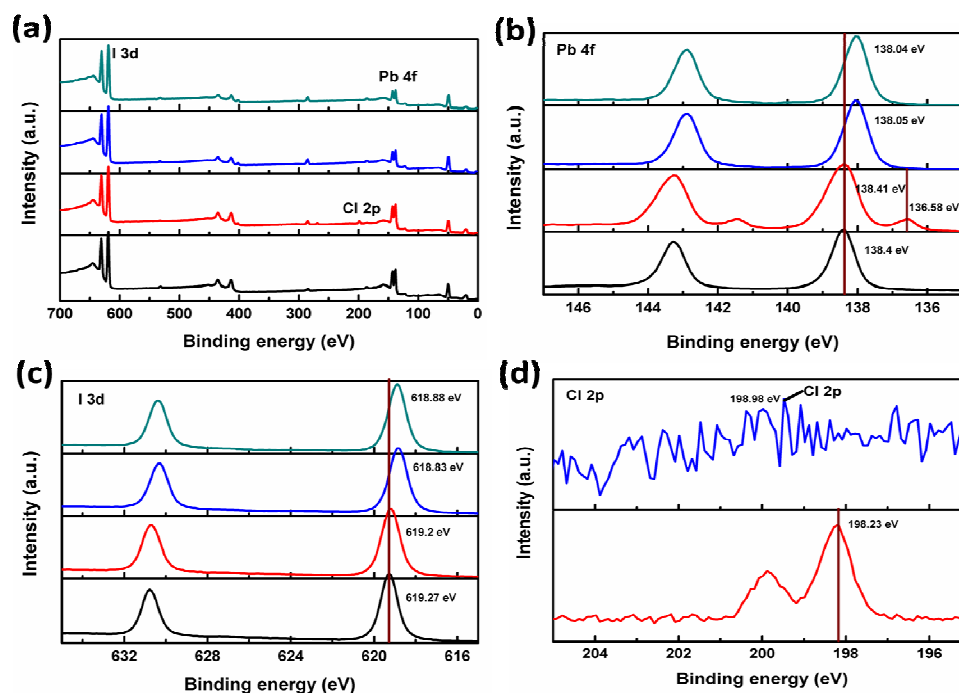
Fig. 4 (a) Overall, (b) Pb4f, and (c) I3d XPS spectra of PbI_2 (black line), $MaPbI_{3-x}Cl_x$ (red line) and $MaPbI_3$ (blue line) films by R2, and $MaPbI_3$ films by R1 (dark cyan); and (d) Cl2p XPS spectra of $MaPbI_{3-x}Cl_x$ seed crystals (bottom) and final $MaPbI_3$ films (upper) by R2.

X-ray photoemission spectroscopy (XPS) spectra are employed. **Fig. 4** shows the (a) Overall, (b) Pb4f, and (c) I3d XPS spectra of PbI_2 (black line), $MaPbI_{3-x}Cl_x$ (red line) and $MaPbI_3$ (blue line) films by R2, and $MaPbI_3$ films by R1 (dark cyan); (d) Cl2p XPS spectra of $MaPbI_{3-x}Cl_x$ seed crystals and final $MaPbI_3$ films by R2. As can be seen, all the signals of C1s, N1s, Pb4f, Pb4P3/2, I3d are detected. When the phase transformation happens, Pb4f and I3d peaks both shift to the lower banding energy side, in agreement with recent reports.[49-51] Notably, the presence of Cl in $MaPbI_{3-x}Cl_x$ seed crystals is strongly verified by the appearance of Cl2p peaks as shown in the bottom portion of **Fig. 4** (d). Intriguingly, signals of Cl2p shown on the upper portion of this plot are almost impossible to distinguish, suggesting only very low Cl content existed in the final $MaPbI_3$ films, which is consistent with above discussion and other related reports.[24,25,52] So we speculate that chemical reaction process in R2 might be as follows:

$$PbI_2 + MaCl\ (g) \longrightarrow MaPbI_{3-x}Cl_x \tag{1}$$

$$MaPbI_{3-x}Cl_x + MaI\ (g) \longrightarrow MaPbI_3 + MaCl\ (g) \uparrow \tag{2}$$
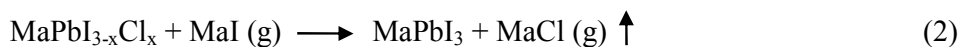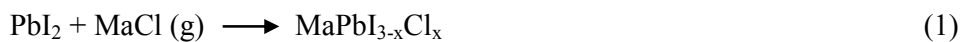
2.3 Film morphology evolution

To gain further insight into the inner reaction process, the film morphology evolution at different reaction stages are also monitored here. **Fig. 5** shows the planar scanning electron microscopy (SEM, ×20 K) images of (a) PbI_2, (b) $MaPbI_{3-x}Cl_x$ and (c) $MaPbI_3$ films by R2, and (d) $MaPbI_3$ films by R1. The low-magnification (×10 K) SEM pictures are provided in **Fig. S2**. Meanwhile, their corresponding 2-D and 3-D atomic force microscopy (AFM) height images are also shown in **Fig. S3** and **Fig. 6**, respectively. In general, PbI_2 is selected to prepare precursor films in terms of its relatively high solubility in Dimethylformamide (DMF) solvent compared with that of $PbCl_2$.[29] Unfortunately, several unsolved problems exist in the PbI_2 system, such as
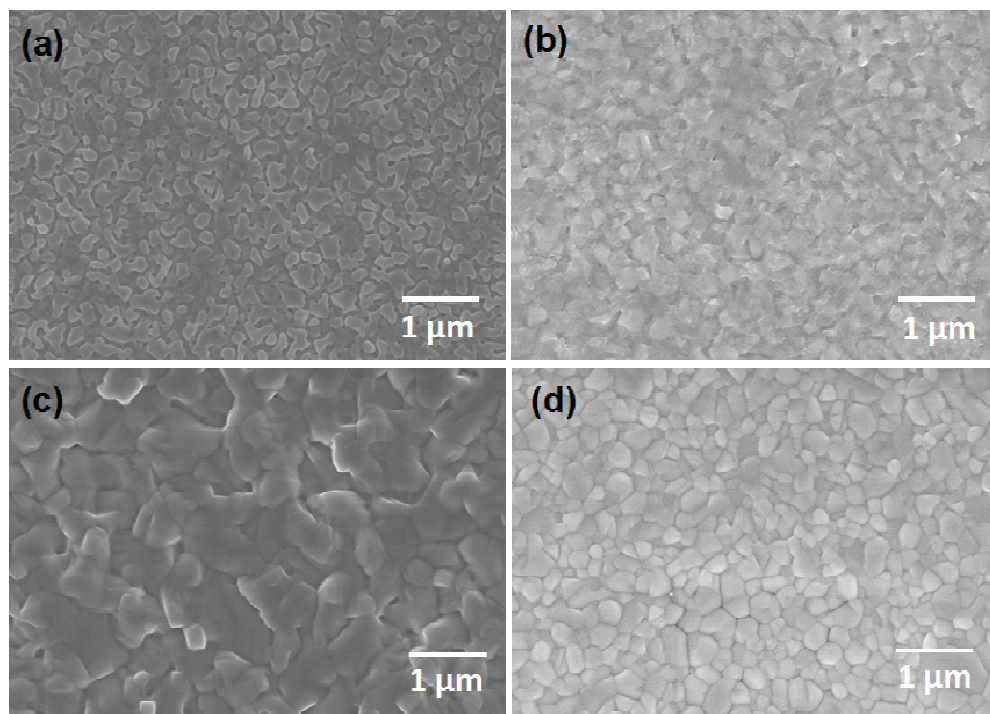

Fig. 5 Planar SEM (× 20 K) images of (a) PbI_2, (b) $MaPbI_{3-x}Cl_x$ and (c) $MaPbI_3$ films by R2, and (d) $MaPbI_3$ films by R1.

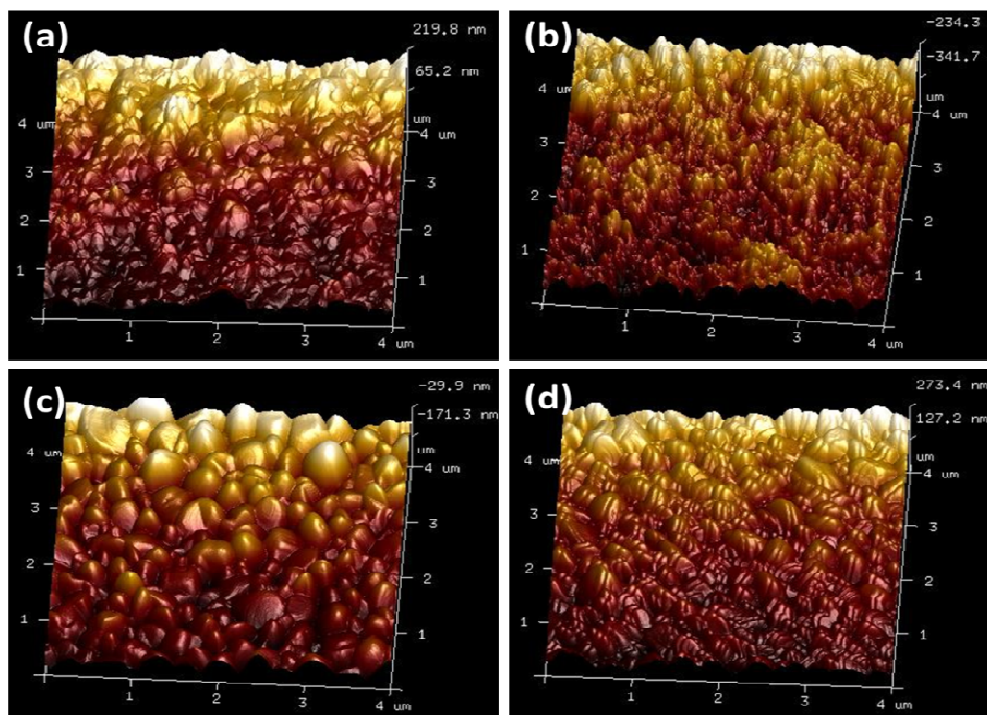**Fig. 6** The 3-D height images (4 × 4 μm) of (a) PbI_2, (b) $MaPbI_{3-x}Cl_x$ and (c) $MaPbI_3$ films by R2, and (d) $MaPbI_3$ films by R1.

large amounts of colloid suspensions, the presence of needle-shaped solvation intermediates, and the over-rapid crystallization nature.[32-36] A few fruitful works have confirmed that the poor quality of PbI_2 films is the culprit, which usually leads to the uneven and porous $MaPbI_3$ layers with incomplete conversion.[33,53] Here from the images of PbI_2 films, irregular polyhedron shape grains with different sizes of 100~300 nm are observed on the substrate. It is apparent that PbI_2 film surface is crisscrossed by irrigation canals and ditches, as clearly shown in **Fig. S4**, which might be caused from the volatilization of DMF during the spin-coating and hot treatment process. Worse yet is that, these inherent ditch defects would seriously destroy the uniformity of the final perovskite films if as-obtained PbI_2 was directly employed as growth templates. Thus it is not strange that the uneven $MaPbI_3$ films by R1 in **Fig. 5** (d) are composed of many small grains, accompanying with apparent avoids and cracks. The poor film quality generally results in a low V_{oc} of 0.85~0.95 V and heavy

deterioration on its PV performance.[39-42,54,55] Strikingly, from the morphology of MaPbI$_{3-x}$Cl$_x$ films as shown in **Fig. 5** (b), we surprisingly find that the inherent canals and ditches on PbI$_2$ templates are successfully repaired by the introduced MaCl vapor. Comparing **Fig. 6** (a, b) and **Fig. S3** (a, b), it is apparent that PbI$_2$ grains become small and the inherent ditches are totally disappeared. Thus, through this special grain refining process, closely packed MaPbI$_{3-x}$Cl$_x$ seed crystals come into being. With the aid of Cl-conducted defect-healing ability, smooth and continuous MaPbI$_{3-x}$Cl$_x$ seed films with full coverage are obtained, as shown in **Fig. 6** (b). Then, the well-defined small seeds grow up to be compact, uniform MaPbI$_3$ perovskite layers without any cracks or voids, as observed in **Fig. 5** (c). From **Fig. 5** (c) and (d), **Fig. 6** (c) and (d), and **Fig. S3** (c) and (d), under the identical reaction temperature and time, perovskite grains from seed-mediated R2 are much larger, denser, and more uniform than that of R1. So our method is able to achieve high-quality perovskite films via a Cl-conducted defect-healing and seed crystal-mediated growth process.

   Fig. 7 provides particle size distributions of MaPbI$_3$ films by R2 and R1 based on their SEM images in **Fig. 2** (c) and (d), respectively. For quantitatively showing
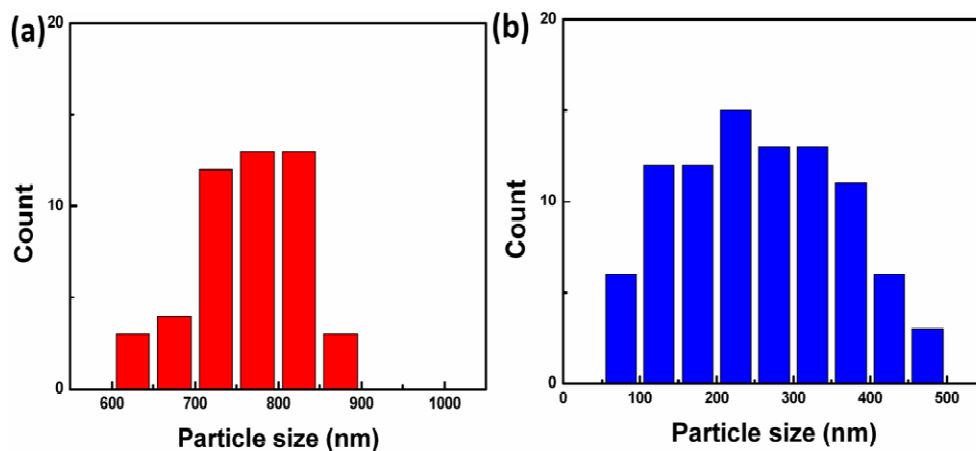

Fig. 7 Particle size distributions of MaPbI$_3$ films by (a) R2 and (b) R1 based on their SEM images in Figure 2 (c) and (d), respectively.

the uniformity of as-prepared perovskite films, herein Nano Measure software is used to analyze the particle size distribution as reported method,[33] and all the grains in **Fig. 2** (c) and 90 pieces of grains in **Fig. 2** (d) are precisely counted. As calculated in the plots, perovskite films by R1 are composed of discretely distributed grains with sizes from 50 nm to 500 nm; while highly crystalized R2 films have a narrow distribution with larger grain sizes around 80% located in the small range of 700~850 nm. As previous reports, the average grain sizes of MaPbI$_3$ films by vapor-assisted approaches are usually below 500 nm.[39,41,42] Here we can see that the grain sizes in R2 grow up to be micron level, which could effectively reduce the charge recombination in GBs and enhance the PV performance. Therefore, it can be concluded that perovskite films from STCVD possess larger grains, narrower distributions, and better uniformities than that of R1, which indicates that closely packed MaPbI$_{3-x}$Cl$_x$ seed crystals play a crucial role during G-S growth process. In addition, it is found that almost 45% of I are replaced by Cl in MaPbI$_{3-x}$Cl$_x$ from SEM-EDS (**Fig. S5).** Similarly, the Cl content in the final perovskites is not detectable. This is according with other studies, and we speculate that Cl might volatilize as MaCl gas via the above-deduced reaction process (1) and (2).[24,52] In brief, compact, crack-free, and highly uniform MaPbI$_3$ layers with large grains are obtained via STCVD approach, and its film quality is much better than that of by the traditional vapor-assisted method. Importantly, a novel defect repairment and seed crystal-mediated growth behavior is first discovered, and the exact role of Cl in morphological evolution during G-S growth process is also revealed here.

2.4 Device performances of PSCs

The planar PSCs based on MaPbI$_3$ films by common CVD in R1 and our STCVD in R2 are separately fabricated, and their device performances including *PCE*

and stability properties are examined as well. Strikingly, from the low- and high-magnification cross-sectional SEM images of PSCs by STCVD as shown in **Fig. 8** (a) and (b), we can see that massive crystal grains with a straightforward long-distance uniformity are full-covered on the TiO_2/FTO/Glass substrate. Such high-quality perovskite layers with ultra-large and super-dense grains are extremely rare in solution process or vapor-assisted approach, which are even comparable with that of by vacuum evaporation method. Bi *et al.* have illustrated that large-aspect-ratio grains are required in polycrystalline thin-film PVs for the reduction of charge recombination at GBs and the enhancement of *PCE*.[56] Thus, the nearly-flawless high film quality is expected to promote its device performances.

Then, we compare their device PV performances of PSCs by R1 and R2 measured without aperture mask as listed in **Tab. 1**. The current density-voltage (*J-V*) curves and external quantum efficiency (*EQE*) spectra are shown in **Fig. 8** (c) and (d), respectively. Generally, PSCs by vapor-assisted method usually have a relatively low V_{oc} around 0.9 V.[39-42] Thus solar cells by R1 only give a low mean efficiency of 8.39% with the V_{oc} of 0.915 V, short current density (J_{sc}) of 16.62 mA/cm^2, and filling factor (*FF*) of 55.68. The best efficiency by R1 is only just 10.29%. In contrast, an average efficiency of PSCs by R2 greatly increases to 11.52% (V_{oc}: 0.942 V; J_{sc}: 18.80 mA/cm^2; *FF*: 58.10), increased by almost 40% compared with that of by R1. Notably, owning to the large and crack-free grains in R2, V_{oc} is greatly improved from 0.915 V

Tab.1 PV performance data for PSCs. Each value represents the average from ten cells.

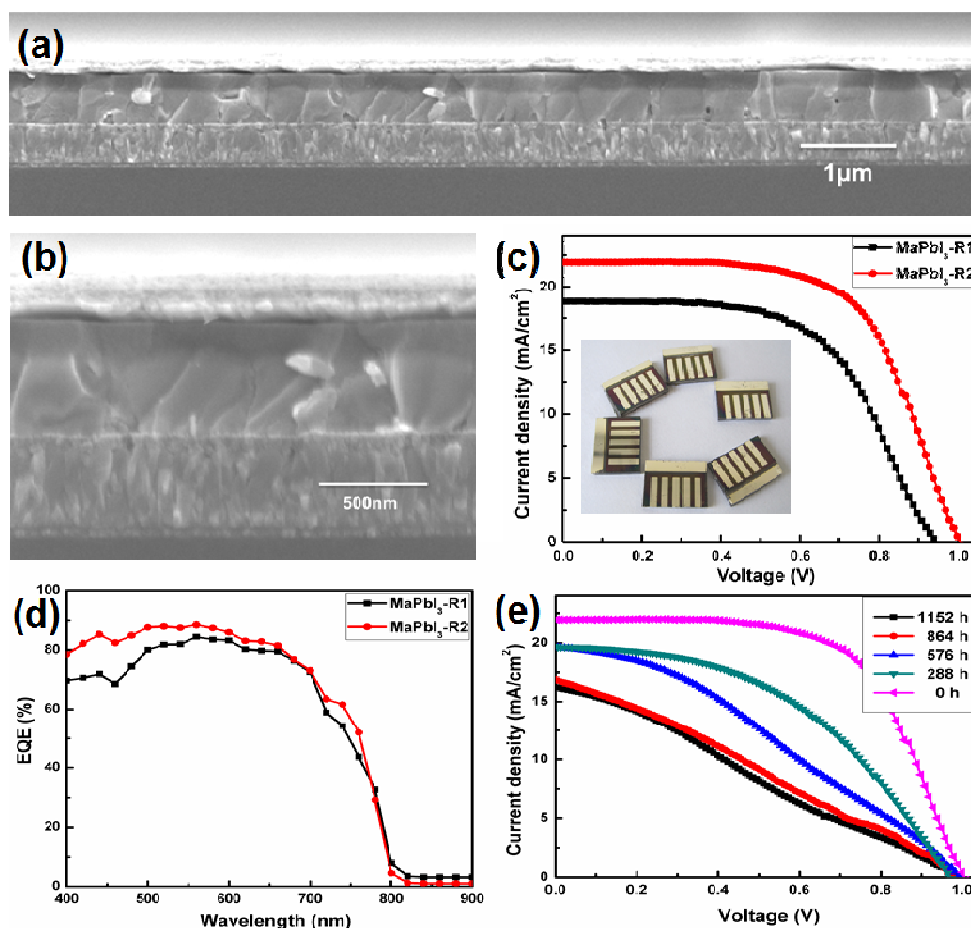| Method	V_{oc} (V)	J_{sc} (mA/cm^2)	FF	PCE (%) [Best-PCE]
R1	0.915±0.038	16.62±2.71	55.68±7.99	8.39 [10.29]
R2	1.001±0.008	20.13±1.87	57.45±3.44	11.52 [13.76]

Fig. 8 (a) Low- and (b) high-magnification SEM images of the R2 device; (c) *J-V* curves inserted with device photographs and (d) *EQE* spectra of R1 and R2 PSCs; (e) *J-V* curves of R2 PSCs stored under ambient conditions over different times: 0 hour, 288 hour, 576 hour, 864 hour, and 1152 hour, giving efficiencies of 13.76%, 8.72%, 6.35%, 4.58%, and 4.15%, respectively.

to 1.001 V, with an enhancement of 86 mV. Our champion cells provide a high efficiency of 13.76% (V_{oc}: 1.005 V; J_{sc}: 21.94 mA/cm^2; *FF*: 62.40), with big V_{oc} exceeding 1.0 V and J_{sc} approaching 22 mA/cm^2. To the best of our knowledge, this is one of the highest PCE reports by CVD approaches so far. Simultaneously, PSCs by R2 have higher *EQE* values over the whole visible spectral range than that of R1, leading to the great enhancement of J_{sc}, which must be beneficial from the higher film quality. In addition, the reverse and forward scan J-V characteristics are also examined to investigate the hysteresis effect, which is reported to be heavily existed in the planar structural PSCs.[57] So we select a representative cell to test this effect. As

shown in **Fig. S6**, the PSCs in the reverse scan give the PCE of 12.29% with J_{sc} of

20.16 mA/cm^2, V_{oc} of 1.002 V, and *FF* of 60.84%, and PSCs in the forward scan show

the PCE of 9.67% with J_{sc} of 20.25 mA/cm^2, V_{oc} of 1.019 V, and *FF* of 46.86%. Thus

it still exhibits a hysteresis phenomenon, which might be relieved through the

efficient charge extraction via further morphological and structural optimization.

Finally, the device stability of as-fabricated PSCs is examined. Basically,

efficient perovskite device should meet the requirement for stability before it can be

really applied in outdoor environments. In terms of the fast degradation nature of

PSCs in most solution process cases, however, limited studies are focused on this

important issue.[58-60] As shown in **Fig. 8** (e), the stability of our R2 PSCs without

encapsulation stored under dark in ambient air over different times is tested.

Surprisingly, they still have an efficiency of 4.15% even undergoing upon exposure to
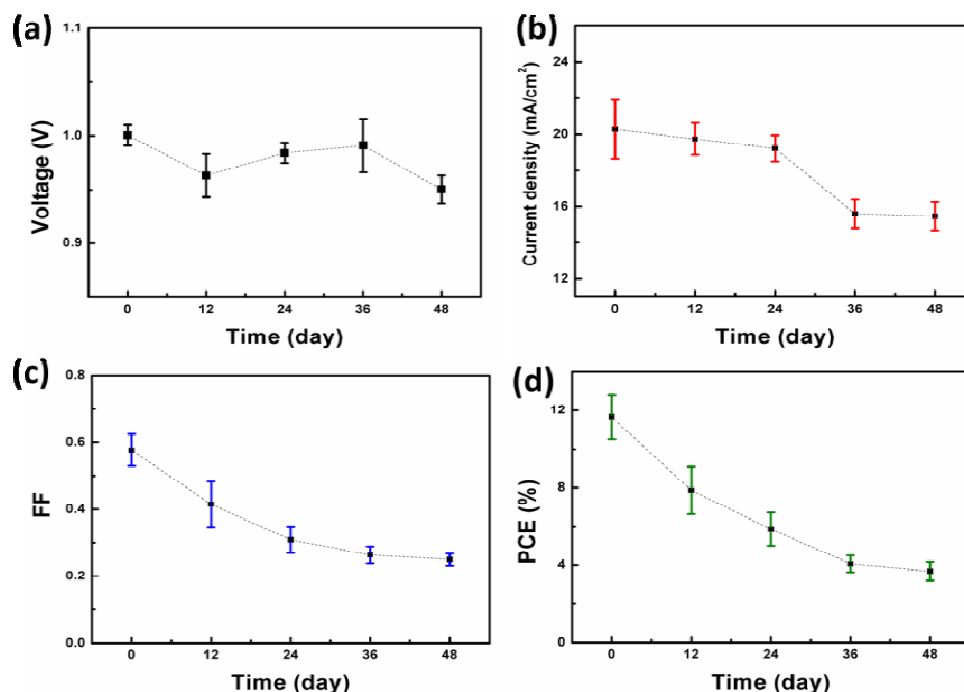

Fig. 9 Stability research on eight PSCs without encapsulation stored under dark in ambient air over different times: 0 hour (0 day), 288 hour (12 day), 576 hour (24 day), 864 hour (36 day), and 1152 hour (48 day), respectively.

the ambient conditions for 1152 hour. **Fig. 9** shows the stability of eight PSCs

reserved in air with different days: 0 hour (0 day), 288 hour (12 day), 576 hour (24

day), 864 hour (36 day), and 1152 hour (48 day), respectively. It can be observed that

V_{oc} and J_{sc} only decline a little; just *FF* drops drastically, which might be caused by

the hygroscopicity of spiro- MeOTAD hole-transporting layer. Inversely, device by R1

deteriorates very fast, and only can be stored for several days. After exposing for 48

day visible in **Fig. S7** (a, b), it is obvious that device by R1 is totally destroyed, while

there is no apparent change in the appearance of R2 cells. Because the compact

perovskite structure in our PSCs is hard to be decomposed by the air moisture, thus it

exhibits a good stability feature.

3. Conclusions

In summary, a novel Cl-incorporated STCVD method is developed to realize the

controllable preparation of PSCs, and the Cl-conducted defect-healing and seed

crystal-assisted growth phenomenon is first reported here. We find that Cl has an

ultra-strong reaction capacity with PbI_2 and also owns a special grain refining ability,

which could effectively heal the inherent ditch defects on PbI_2 templates, and generate

continuous $MaPbI_{3-x}Cl_x$ seed films with complete conversion. With the aid of seed

crystals, super-dense, crack-free, and highly uniform $MaPbI_3$ layers with micron-level

large grains are obtained. As a consequence, the device PV performance via STCVD

is significantly enhanced comparing with that of by the common CVD. Accordingly,

the device V_{oc} boosts from 0.915 V to 1.001 V, with an impressive enhancement of 86

mV; and the best efficiency is greatly improved from 10.29% to 13.76%,

demonstrating a high efficiency among CVD processed PSCs. Therefore, our

proprietary STCVD method possessing low cost, high efficiency, and stable feature,

shows high potential to be applied in the commercial production of PSCs. Meanwhile, our research also provides a new insight on the function of Cl during G-S growth process of perovskite materials.

4. Experimental

4.1 Materials

All materials were purchased from Aladdin, unless otherwise specified, and they were used as received. Spiro-MeOTAD was a Derthon product and FTO glasses of 2.2 mm thickness and 15 Ω/square were purchased from Pilkington.

4.2 MaI and MaCl synthesis

MaI and MaCl were prepared according to previous reports.[41] MaI was synthesized by reacting methylamine (33 wt% ethanol solution) and hydroiodic acid (45 wt% in water) with the molar ratio of 1.2:1 in an ice-bath with continuous stirring. Then the precipitate was washed with diethyl ether three times and finally dried at 60 ^{o}C in a vacuum oven for 24 hour. MaCl was synthesized using hydrocholoride acid (37 wt% in water) with the same molar ratio and synthesizing conditions of MaI.

4.3 Fabrication of PSCs

Firstly, TiO_2 compact layers were obtained by spin-coating a mildly acidic solution of titanium isopropoxide in ethanol at 2000 rpm for 60 s, then annealed at 500 ^{o}C for 30 min, and treated in 40 mM aqueous solution of TiCl4 at 65 ^{o}C for 30 min, following dried at 500 ^{o}C for another 30 min. Secondly, PbI_2 powder was dissolved in N,N-dimethylformamide (DMF) with a concentration of 400 mg/mL. PbI_2 films were coated by spin-coating as-synthesized solution on TiO_2/FTO/Glass substrate at a speed of 4000 rpm for 30 s. Thirdly, PbI_2 films were placed into the

tubular quartz furnace. In route i (R1), PbI_2 directly reacted with MaI at 145 ^{o}C for 100 min; While in route ii (R2), it first reacted with MaCl at 120 ^{o}C for 5 min, and then reacted with MaI at 145 ^{o}C for 100 min. After the reaction, $MaPbI_3$ films were taken out and washed with isopropanol, following annealed at 145 ^{o}C for 30 min in air. Finally, hole-transporting layer was deposited by spin coating with a speed of 4000 rpm for 30 s. And the solution was synthesized by dissolving 72.3 mg spiro-MeOTAD, 17.5 µL of lithium bis(trifluoromethanesul-fonyl)imide solution (520 mg LITSFI in 1 mL acetonitrile) and 28.8 µL 4-tert-butylpyridine in 1 mL chlorobenzene. Then silver electrode was evaporated by thermal vacuum evaporation at 10^{-6} bar with a stainless steel mask (active area: 0.12 cm^2). All the experiments were carried out under fully open-air conditions with humidity around 40%.

4.4 Characterizations

The current density-voltage (*J-V*) curves were measured using a solar simulator (Newport, Oriel Sol3A 94023A) with a source meter (Keithley 2400) under 100 $mWcm^{-2}$ illumination (AM 1.5G) and tested without aperture mask. The step voltage was fixed at 10 mV and the active area of single cells is 0.12 cm^2. *EQE* was measured with a Newport *QE* measurement kit (IQE-200) by focusing a monochromatic beam of light onto the devices. The crystal structures of the perovskite films were measured by X-ray diffraction (D/MAX 2500V). The morphology and composition were separately observed by field emission scanning electron microscope (FESEM, Sirion 200), atomic force microscope (AFM, Dimension FastScan), and SEM-EDS. The absorption spectrum was recorded by UV-visible spectrophotometer (CARY 5000) with the wavelength range of 300~1000 nm. X-Ray photoelectron spectroscopy (XPS) was measured with an ESCALAB 250 instrument.

Supporting Information

Acknowledgments

Notes and references

1   D. J. Norris, E. S. Aydil, *Science*, 2012, **338**, 625-626.

2   Z. Liu, D. Guan, D. Crawford-Brown, Q. Zhang, K. He, J. Liu, *Nature*, 2013, **500**, 143-145.

3   A. Chirila, P. Reinhard, F. Pianezzi, P. Bloesch, A. R. Uhl, C. Fella, L. Kranz, D. Keller, C. Gretener, H. Hagendorfer, D. Jaeger, R. Erni, S. Nishiwaki, S. Buecheler, A. N. Tiwari, *Nature Mater.*, 2013, **12**, 1107-1111.

4   M. A. Green, K. Emery, Y. Hishikawa, W. Warta, E. D. Dunlop, *Prog. Photovolt.*, 2015, **23**, 1-9.

5   N. J. Jeon, J. H. Noh, Y. C. Kim, W. S. Yang, S. Ryu, S. I. Seok, *Nat. Mater*., 2014, **13**, 897-903.

6   K. Wojciechowski, M. Saliba, T. Leijtens, A. Abate, H. J. Snaith, *Energy Environ. Sci.*, 2014, **7**, 1142-1147.

7   N. J. Jeon, H. G. Lee, Y. C. Kim, J. Seo, J. H. Noh, J. Lee, S. I. Seok, *J. Am. Chem. Soc.*, 2014, **136**, 7837-7840.

8   S. T. Ha, X. Liu, Q. Zhang, D. Giovanni, T. C. Sum, Q. Xiong, *Adv. Opt. Mater.*, 2014, **2**, 838-844.

9   P. Liang, C. Chueh, X. Xin, F. Zuo, S. T. Williams, C. Liao, and A. Jen, *Adv. Energ. Mater.*, 2015, **5**, 1400960.

10 A. Kojima, K. Teshima, Y. Shirai, T. Miyasaka, *J. Am. Chem. Soc.*, 2009, **131**, 6050-6051.

11 H. Zhou, Q. Chen, G. Li, S. Luo, T. B. Song, H. S. Duan, Z. Hong, J. You, Y. Liu, Y. Yang, *Science*, 2014, **345**, 542-546.

12 W. Nie, H. Tsai, R. Asadpour, J. C. Blancon, A. J. Neukirch, G. Gupta, J. J. Crochet, M. Chhowalla, S. Tretiak, M. A. Alam, H. L. Wang, A. D. Dohite, *Science*, 2015, **347**, 522-525.

13 F. Wang, H. Yu, H. Xu, N. Zhao, *Adv. Funct. Mater.*, 2015, **25**, 1120-1126.

14 D. Liu, J. Yang, T. L. Kelly, *J. Am. Chem. Soc.*, 2014, **136**, 17116-17122.

15 N. J. Jeon, J. H. Noh, W. S. Yang, Y. C. Kim, S. Ryu, J. Seo, S. I. Seok, *Nature*, 2015, **517**, 476-480.

16 X. Xu, Z. Liu, Z. Zuo, M. Zhang, Z. Zhao, Y. Shen, H. Zhou, Q. Chen, Y. Yang, M. Wang, *Nano Lett.*, 2015, **15**, 2402-2408.

17 W. S. Yang, J. H. Noh, N. J. Jeon, Y. C. Kim, S. Ryu, J. Seo and S. I. Seok, *Science*, 2015, aaa9272.

18 G. E. Eperon, V. M. Burlakov, P. Docampo, A. Goriely, H. J. Snaith, *Adv. Funct. Mater.*, 2014, **24**, 151-157.

19 J. J. Choi, X. Yang, Z. M. Norman, S. J. L. Billinge, J. S. Owen, *Nano Lett.*, 2014, **14**, 127-133.

20 A. Dualeh, N. Tetreault, T. Moehl, P. Gao, M. K. Nazeeruddin, M. Gratzel, *Adv. Funct. Mater.*, 2014, **24**, 3250-3258.

21 M. Saliba, K. W. Tan, H. Sai, D. T. Moore, T. Scott, W. Zhang, L. A. Estroff, U. Wiesner, H. J. Snaith, *J. Phys. Chem. C*, 2014, **118**, 17171-17177.

22 M. M. Lee, J. Teuscher, T. Miyasaka, T. N. Murakami, H. J. Snaith, *Science*, 2012, **338**, 643-647.

23 S. D. Stranks, G. E. Eperon, G. Grancini, C. Menelaou, M. J. P. Alcocer, T. Leijtens, L. M. Herz, A. Petrozza, H. J. Snaith, *Science*, 2013, **342**, 341-344.

24 S. Colella, E. Mosconi, P. Fedeli, A. Listorti, F. Gazza, F. Orlandi, P. Ferro, T. Besagni, A. Rizzo, G. Calestani, G. Gigli, F. D. Angelis, R. Mosca, *Chem. Mater.*, 2013, **25**, 4613-4618.

25 E. L. Unger, A. R. Bowring, C. J. Tassone, V. L. Pool, A. G. Parker, R. Cheacharoen, K. H. Stone, E. T. Hoke, M. F. Toney, M. D. McGehee, *Chem. Mater.*, 2014, **26**, 7158-7165.

26 Q. Chen, H. Zhou, Y. Fang, A. Z. Stieg, T. Song, H. Wang, X. Xu, Y. Liu, S. Lu, J. You, P. Sun, J. McKay, M. S. Goorsky, Y. Yang, *Nature comm.*, 2015, **6**, 7269.

27 Y. Zhao, K. Zhu, *J. Phys. Chem. C*, 2014, **118**, 9412-9418.

28 Y. Li, W. Sun, W. Yan, S. Ye, H. Peng, Z. Liu, Z. Bian, C. Huang, *Adv. Funct. Mater.*, 2015, **25**, 4867-4873.

29 M. Jiang, J. Wu, F. Lan, Q. Tao, G. Li, *J. Mater. Chem. A*, 2015, **3**, 963-967.

30 N. Yantara, F. Yanan, C. Shi, H. A. Dewi, P. P. Boix, S. G. Mhaisalkar, N. Mathews, *Chem. Mater.*, 2015, **27**, 2309-2314.

31   Q. Dong, Y. Yuan, Y. Shao, Y. Fang, Q. Wang, J. Huang, *Energy Environ. Sci.*, 2015, **8**, 2464-2470.

32   Y. Tidhar, E. Edri, H. Weissman, D. Zohar, G. Hodes, D. Cahen, B. Rybtchinski, S. Kirmayer, *J. Am. Chem. Soc.*, 2014, **136**, 13249-13256.

33   Y. Wu, A. Islam, X. Yang, C. Qin, J. Liu, K. Zhang, W. Peng, L. Han, *Energy Environ. Sci.*, 2014, **7**, 2934-2938.

34   F. Hao, C. C. Stoumpos, Z. Liu, R. P. H. Chang, M. G. Kanatzidis, *J. Am. Chem. Soc.*, 2014, **136**, 16411-16419.

35   H. Yu, F. Wang, F. Xie, W. Li, J. Chen, N. Zhao, *Adv. Funct. Mater.*, 2014, **24**, 7102-7108.

36   S. T. Williams, F. Zuo, C.-C. Chueh, C.-Y. Liao, P.-W. Liang, K.-Y. Jen, *ACS nano*, 2014, **8**, 10640-10654.

37   M. Liu, M. B. Johnston, H. J. Snaith, *Nature*, 2013, **501**, 395-398.

38   C. W. Chen, H. W. Kang, S. Y. Hsiao, P. F. Yang, K. M. Chiang, H. W. Lin, *Adv. Mater.*, 2014, **246**, 6647-6652.

39   Q. Chen, H. Zhou, Z. Hong, S. Luo, H. S. Duan, H. H. Wang, Y. Liu, G. Li, Y. Yang, *J. Am. Chem. Soc.*, 2014, **136**, 622-625.

40   M. R. Leyden, L. K. Ono, S. R. Raga, Y. Kato, S. Wang, Y. Qi, *J. Mater. Chem. A*, 2014, **2**, 18742-18745.

41   P. Luo, Z. Liu, W. Xia, C. Yuan, J. Cheng, Y. Lu, *ACS Appl. Mater. Interfaces*, 2015, **7**, 2708-2714.

42   P. Luo, Z. Liu, W. Xia, C. Yuan, J. Cheng, Y. Lu, *J. Mater. Chem. A*, 2015, **3**, 12443-12451.

43   M. R. Leyden, M. V. Lee, S. R. Raga, Y. Qi, *J. Mater. Chem. A*, 2015, **3**, 16097-16103.

44   B. W. Park, E. M. J. Johansson, B. Philippe, T. Gustafsson, K. Sveinbjornsson, A. Hagfeldt, G. Boschloo, *Chem. Mater.*, 2014, **26**, 4466-4471.

45   C. Liu, J. Fan, X. Zhang, Y. Shen, L. Yang, Y. Mai, ACS *Appl. Mater. Interfaces*, 2015, **7**, 9066-9971.

46   E. Mosconi, A. Amat, K. Nazeeruddin, M. Gra, F. De. Angelis, *J. Phys. Chem. C*, 2013, **117**, 13902-13913.

47   Wyckoff, G. R. W. *New York Note: Cadmium Iodide Structure*, Interscience publishers, New York, 1963.

48   S. Sasaki, C. T. Prewitt, J. D. Bass, W. A. Schulze, *Acta Cryst.*, 1987, **43**, 1668-1674.

49   R. Lindblad, D. Bi, B. W. Park, J. Oscarsson, M. Gorgoi, H. Siegbahn, M. Odelius, E. M. J. Johansson, H. Rensmo, *J. Phys. Chem. Lett.*, 2014, **5**, 648-653.

50   S. R. Raga, M. C. Jung, M. V. Lee, M. R. Leyden, Y. Kato, Y. Qi, *Chem. Mater.*, 2015, **27**, 1597-1603.

51 F. Xie, D. Zhang, H. Su, X. Ren, K. S. Wong, M. Gratzel, W. C. H. Choy, *ACS Nano*, 2015, **9**, 639-646.

52 Y. Li, J. K. Cooper, R. Buonsanti, C. Giannini, Y. Liu, F. M. Toma, I. D. Sharp, *J. Phys. Chem. Lett.*, 2015, **6**, 493-499.

53 C.-G. Wu, C.-H. Chiang, Z.-L. Tseng, M. K. Nazeeruddin, A. Hagfeldt, M. Gratzel, *Energy Environ. Sci.*, DOI: 10.1039/C5EE00645G.

54 H. S. Ko, J. W. Lee, N. G. Park, *J. Mater. Chem. A*, 2015, **3**, 8808-8815.

55 J. H. Im, I. H. Jang, N. Pellet, M. Gratzel, N. G. Park, *Nat. Nanotechnol.*, 2014, **9**, 927-932.

56 C. Bi, Q. Wang, Y. Shao, Y. Yuan, Z. Xiao, J. Huang, *Nature comm.*, 2015, **6**, 7747.

57 Y. Li, J. K. Cooper, R. Buonsanti, C. Giannini, Y. Liu, F. M. Toma, I. D. Sharp, *J. Phys. Chem. Lett.* 2015, **6**, 493-499.

58 G. Niu, L. Wang, *J. Mater. Chem. A*, 2015, **3**, 8970-8980.

59 N. Tripathi, M. Yanagida, Y. Shirai, T. Masuda, L. Han, K. Miyano, *J. Mater. Chem. A*, 2015, **3**, 12081-12088.

60 F. K. Aldibaja, L. Badia, E. M.-Marzá, R. S. Sánchez, E. M. Barea, I. M.- Sero, *J. Mater. Chem. A*, 2015, **3**, 9194-9200.

Text:

A facile MaCl-assisted STCVD method is developed, and the novel defect repairment and seed crystal-mediated growth behavior is first reported.

Table of Content (TOC):